
ANTN: Bridging Autoregressive Neural Networks and Tensor Networks for Quantum Many-Body Simulation

Zhuo Chen¹² Laker Newhouse^{3*} Eddie Chen^{4*} Di Luo^{125†} Marin Soljačić⁴

¹NSF AI Institute for Artificial Intelligence and Fundamental Interactions

²Center for Theoretical Physics, Massachusetts Institute of Technology

³Department of Mathematics, Massachusetts Institute of Technology

⁴Department of Physics, Massachusetts Institute of Technology

⁵Department of Physics, Harvard University

{chenzhuo,lakern,ezchen,diluo,soljacic}@mit.edu

Abstract

Quantum many-body physics simulation has important impacts on understanding fundamental science and has applications to quantum materials design and quantum technology. However, due to the exponentially growing size of the Hilbert space with respect to the particle number, a direct simulation is intractable. While representing quantum states with tensor networks and neural networks are the two state-of-the-art methods for approximate simulations, each has its own limitations in terms of expressivity and inductive bias. To address these challenges, we develop a novel architecture, Autoregressive Neural TensorNet (ANTN), which bridges tensor networks and autoregressive neural networks. We show that Autoregressive Neural TensorNet parameterizes normalized wavefunctions, allows for exact sampling, generalizes the expressivity of tensor networks and autoregressive neural networks, and inherits a variety of symmetries from autoregressive neural networks. We demonstrate our approach on quantum state learning as well as finding the ground state of the challenging 2D J_1 - J_2 Heisenberg model with different systems sizes and coupling parameters, outperforming both tensor networks and autoregressive neural networks. Our work opens up new opportunities for scientific simulations of quantum many-body physics and quantum technology.

1 Introduction

Quantum many-body physics is fundamental to our understanding of the universe. It appears in high energy physics where all the fundamental interactions in the Standard Model, such as quantum electrodynamics (QED) and quantum chromodynamics (QCD), are described by quantum mechanics. In condensed matter physics, quantum many-body physics has led to a number of rich phenomena and exotic quantum matters, including superfluids, superconductivity, the quantum Hall effect, and topological ordered states (Girvin & Yang, 2019). As an application, quantum many-body physics is crucial for new materials design. The electronic structure problem and chemical reactions in quantum chemistry are governed by quantum many-body physics. The recent development of quantum computers is also deeply connected to quantum many-body physics. A multi-qubit quantum device is intrinsically a quantum many-body system, such that progress on quantum computer engineering is tied to our understanding of quantum many-body physics (Preskill, 2021).

*equal contribution

†corresponding author

All information of a closed quantum many-body system is captured by the wavefunction, whose properties are described by the famous Schrödinger equation. An important tool to study and understand quantum many-body physics is to classically simulate the wavefunction. However, the wavefunction is a high dimensional function in Hilbert space, whose dimension grows exponentially with the number of particles. For example, for qubit systems where each qubit has two degrees of freedom, the wavefunction of 300 qubits will have dimension 2^{300} , which is larger than the number of particles in the observable universe. Furthermore, the Schrödinger equation is a complex-valued high-dimensional equation, which is challenging to solve or simulate in general.

A number of algorithms have been developed to simulate quantum many-body physics, including quantum Monte Carlo, tensor networks, neural network quantum states, and direct quantum computation. In particular, computing the ground state of quantum many-body systems is of great interest. One important approach is the variational principle, which provides an upper bound for the ground state energy. To apply variational principle successfully, one must design an ansatz that can represent and optimize the wavefunction efficiently. Tensor networks and neural network quantum states (Carleo & Troyer, 2017) are the two main state-of-the-art methods that can be applied with the variational principle for quantum many-body simulation. However, tensor networks usually suffer from an expressivity issue in systems with more than one dimension, while neural network quantum states usually lack the inductive bias from the underlying physics structure and have sign structure challenges in the representation.

In this paper, we develop a novel architecture, Autoregressive Neural TensorNet (ANTN), to bridge neural network quantum states and tensor networks, achieving the best of both worlds. In particular, our contributions are threefold:

- Develop ANTN with two variants called “elementwise” and “blockwise,” which each naturally generalize the two state-of-the-arts ansatzes, tensor networks (TN) and autoregressive neural networks (ARNN), to provide proper inductive bias and high expressivity.
- Prove that ANTN is normalized with exact sampling, has generalized expressivity of TN and ARNN, and inherits multiple symmetries from ARNN.
- Demonstrate our methods on quantum state learning and variationally finding the ground state of the challenging 2D J_1 - J_2 Heisenberg model, outperforming both TN and ARNN.

2 Related Work

Tensor Networks (TN) represent high-dimensional wavefunctions using low-rank tensor decomposition, notably matrix product state (MPS) (Vidal, 2003, 2004), PEPS (Verstraete & Cirac, 2004), and MERA (Vidal, 2007). They capture the entanglement structure of physical systems and, with algorithms like the density matrix renormalization group (DMRG) (White, 1992), are used for state simulations and real-time dynamics. However, their expressivity can be limited in systems with more than one dimension and systems with high entanglement. In machine learning, TN appears as tensor train (Oseledets, 2011) and CP decomposition methods.

Neural Network Quantum State (NNQS) leverages neural networks for high dimensional wavefunction representation (Carleo & Troyer, 2017). It’s been demonstrated that many quantum states can be approximated or represented by NNQS (Sharir et al., 2021; Gao & Duan, 2017; Lu et al., 2019; Levine et al., 2019a; Luo et al., 2021b,a; Deng et al., 2017; Huang & Moore, 2021; Vieijra et al., 2020), and it has yielded state-of-the-art results in computing quantum system properties (Gutiérrez & Mendl, 2020; Schmitt & Heyl, 2020; Vicentini et al., 2019; Yoshioka & Hamazaki, 2019; Hartmann & Carleo, 2019; Nagy & Savona, 2019; Luo et al., 2021b, 2022a). Key advancements in NNQS include ARNN that improves sample efficiency and gradient estimation, and the development of

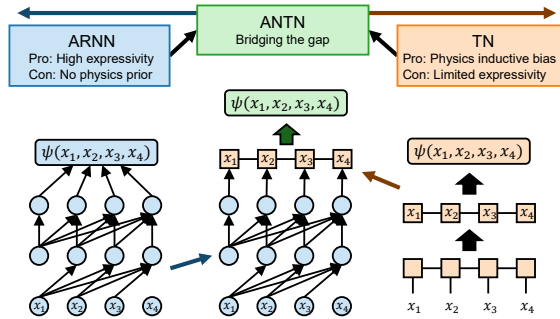


Figure 1: Diagrammatic representation of autoregressive neural network (ARNN), tensor network (TN) and our Autoregressive Neural TensorNet (ANTN).

neural networks that adhere to the underlying symmetries of quantum systems (Luo et al., 2021b; Hibat-Allah et al., 2020; Choo et al., 2019; Luo & Clark, 2019; Hermann et al., 2019; Pfau et al., 2020; Luo et al., 2021a, 2022b, 2021b; Chen et al., 2022). Despite its potential, NNQS faces challenges such as the lack of physics prior and the sign structure problem. While there are attempts to integrate NNQS with TN, including matrix product state with neural network backflow (Lami et al., 2022) and generalizing MPS to RNN (Wu et al., 2022), the former can not produce normalized wavefunctions, while the latter only builds on tensor contractions that lacks the nonlinear activation functions of standard neural network wavefunctions.

3 Background

3.1 Quantum Preliminaries

In this work, we focus on qubit systems in quantum many-body physics. The wavefunction or quantum state ψ of the system is a normalized function $\psi : \mathbb{Z}_2^n \rightarrow \mathbb{C}$ with $\sum_{\mathbf{x}} |\psi(\mathbf{x})|^2 = 1$, where n is the system size. The input to the wavefunction is an n -bit string $\mathbf{x} \in \{0, 1\}^n$. Therefore, the wavefunction ψ can be viewed as a complex-valued vector of size 2^n , with Dirac notation $\langle \psi |$ and $|\psi \rangle$ correspond to a conjugate row vector and a column vector respectively, and $\psi(\mathbf{x}) = \langle \mathbf{x} | \psi \rangle$. Because the size of the wavefunction grows exponentially with the system size n , a direct computation quickly becomes intractable as the system size increases. The goal of NNQS is to design a compact architecture that can approximate and optimize the wavefunction efficiently.

3.2 Quantum State Learning

Given a quantum state $|\phi\rangle$, we are often interested in finding $|\psi_\theta\rangle$ that is closest to $|\phi\rangle$ given the variational ansatz. In quantum mechanics, the closeness of two quantum states are measured by the quantum fidelity $F = |\langle \phi | \psi_\theta \rangle|^2 = |\sum_{\mathbf{x}} \phi^*(\mathbf{x}) \psi_\theta(\mathbf{x})|^2$ where $*$ refers to complex conjugation. Quantum fidelity satisfies $0 \leq F \leq 1$, with $F = 1$ corresponding to exact match, and $F = 0$ orthogonal quantum states. Finding F_{\max} for a given ansatz allows us to quantify how good the ansatz can be used to approximate that state. In practice, minimizing $-\log F$ is usually better than maximizing F itself. This can be achieved by enumerating all the basis \mathbf{x} in small systems and stochastically in large systems such as quantum state tomography (see Appendix A.1).

3.3 Variational Monte Carlo

For a given quantum system with n qubits, the Hamiltonian $\hat{\mathcal{H}}$ can be written as a Hermitian matrix of size $2^n \times 2^n$. The ground state energy E_g of the system is the smallest eigenvalue of $\hat{\mathcal{H}}$ and the ground state is the corresponding eigenvector. For large system sizes, finding the ground state directly is usually impossible. In this case, the variational principle in quantum mechanics provides an upper bound on the ground state energy E_g . For all (normalized) wavefunctions $|\psi\rangle$, it is evident that $E_g \leq \langle \psi | \hat{\mathcal{H}} | \psi \rangle$. Therefore, finding the $|\psi_\theta\rangle$ that minimizes $E_\theta = \langle \psi_\theta | \hat{\mathcal{H}} | \psi_\theta \rangle$ gives the lowest upper bound of the ground state energy. For large system sizes, we can stochastically evaluate and minimize

$$\langle \psi_\theta | \hat{\mathcal{H}} | \psi_\theta \rangle = \sum_{\mathbf{x}\mathbf{x}'} |\psi_\theta(\mathbf{x})|^2 \frac{\mathcal{H}_{\mathbf{x}, \mathbf{x}'} \psi_\theta(\mathbf{x}')}{\psi_\theta(\mathbf{x})} = \mathbb{E}_{\mathbf{x} \sim |\psi_\theta|^2} \frac{\sum_{\mathbf{x}'} \mathcal{H}_{\mathbf{x}, \mathbf{x}'} \psi_\theta(\mathbf{x}')}{\psi_\theta(\mathbf{x})}, \quad (1)$$

where $\mathcal{H}_{\mathbf{x}, \mathbf{x}'}$ refers to the matrix element of $\hat{\mathcal{H}}$ and we interpret $|\psi_\theta(\mathbf{x})|^2$ as a probability distribution. The summation over \mathbf{x}' can be efficiently computed given \mathbf{x} since the Hamiltonian is usually sparse. The gradient $\nabla_\theta E_\theta$ can also be calculated stochastically in a similar fashion (see Appendix A.2).

4 Autoregressive Neural TensorNet (ANTN)

Autoregressive Neural Network Wavefunction. The autoregressive neural network (ARNN) (Fig. 1 left) parameterizes the full probability distribution as a product of conditional probability distributions as

$$p(\mathbf{x}) = \prod_{i=1}^n p(x_i | \mathbf{x}_{<i}), \quad (2)$$

where $\mathbf{x} = (x_1, \dots, x_n)$ is the a configuration of n qubits and $\mathbf{x}_{<i} = (x_1, \dots, x_{i-1})$ is any configuration before x_i . The normalization of the full probability can be guaranteed from the normalization of individual conditional probabilities. The ARNN also allows for exact sampling from the full distribution by sampling sequentially from the conditional probabilities (see Appendix B.1). The autoregressive constructions for probabilities can be easily modified to represent quantum wavefunction by (1) replacing $p(x_i|\mathbf{x}_{<i})$ with a complex valued conditional wavefunction $\psi(x_i|\mathbf{x}_{<i})$ and (2) using the following normalization condition for the conditional wavefunctions: $\sum_x |\psi(x_i|\mathbf{x}_{<i})|^2 = 1$ (Sharir et al., 2020; Hibat-Allah et al., 2020; Luo et al., 2021b). Similar to the case of probabilities, ARNN automatically preserves normalization of wavefunctions and allows for exact sampling (see Appendix B.1). Because of this, ARNN is often more efficient when training and computing various quantum observables compared to other generative neural networks.

Matrix Product State (MPS). MPS (also known as tensor train) is a widely used TN architecture to study quantum many body physics (Vidal, 2003, 2004). The MPS defines a wavefunction using n rank-3 tensors $M_{x_i}^{\alpha_{i-1}\alpha_i}$ with α_{i-1} (or α_i) the index of left (or right) bond dimensions and x_i the configuration of the i th qubit. Then, the full wavefunction is generated by first choosing a particular configuration $\mathbf{x} = (x_1, \dots, x_n)$ and then contracting the tensors selected by this configuration (Fig. 1 right) as

$$\psi(\mathbf{x}) = \sum_{\alpha_1, \dots, \alpha_{n-1}} M_{x_1}^{\alpha_0\alpha_1} \cdots M_{x_n}^{\alpha_{n-1}\alpha_n} = \sum_{\alpha} \prod_{i=1}^n M_{x_i}^{\alpha_{i-1}\alpha_i}, \quad (3)$$

where the left-and-right-most bond dimensions are assumed to be $\mathcal{D}(\alpha_0) = \mathcal{D}(\alpha_{n+1}) = 1$ so are not summed.

Elementwise and Blockwise Construction for ANTN. Both ARNN and MPS are powerful ansatzes for parameterizing quantum many-body wavefunctions. However, they cover different subspaces of the Hilbert space. Albeit very expressive, ARNN lacks the physics prior of the system of interest. In addition, since wavefunctions are complex-valued in general, learning the sign structure can be a nontrivial task (Westerhout et al., 2020). MPS, on the other hand, contains the necessary physics prior and can efficiently represent local or quasi-local sign structures, but its expressivity is severely limited. The internal bond dimension needs to grow exponentially to account for the increase of entanglement. It turns out that MPS representation is not unique that many MPS actually represents the same wavefunction; and if we choose a particular constraint (without affecting the expressivity), MPS allows for efficient evaluation of conditional probability and exact sampling (Ferris & Vidal, 2012) (see Appendix B.2). Because both these ansatzes allow for exact sampling, it is natural to combine them to produce a more powerful ansatz. Therefore, we develop the Autoregressive Neural TensorNet (ANTN) (Fig. 1 (middle)). In the last layer of the ANTN, instead of outputting the conditional wavefunction $\psi(x_i|\mathbf{x}_{<i})$, we output a conditional wavefunction tensor $\tilde{\psi}_L^{\alpha_{i-1}\alpha_i}(x_i|\mathbf{x}_{<i})$ for each site. Defining the left partially contracted tensor up to qubit j as $\tilde{\psi}_L^{\alpha_j}(\mathbf{x}_{\leq j}) := \sum_{\alpha_{<j}} \prod_{i=1}^j \tilde{\psi}^{\alpha_{i-1}\alpha_i}(x_i|\mathbf{x}_{<i})$, we can define the (unnormalized) marginal probability distribution as

$$q(\mathbf{x}_{\leq j}) := \sum_{\alpha_j} \tilde{\psi}_L^{\alpha_j}(\mathbf{x}_{\leq j}) \tilde{\psi}_L^{\alpha_j}(\mathbf{x}_{\leq j})^*, \quad (4)$$

where $*$ denotes complex conjugation. Then, the (normalized) conditional probability can be obtained as $q(x_j|\mathbf{x}_{<j}) = q(\mathbf{x}_{\leq j}) / \sum_{x_j} q(\mathbf{x}_{\leq j})$. We construct the overall wavefunction by defining both its amplitude and phase according to

$$\psi(\mathbf{x}) := \sqrt{q(\mathbf{x})} e^{i\phi(\mathbf{x})}, \quad (5)$$

with $q(\mathbf{x}) := \prod_{i=1}^n q(x_i|\mathbf{x}_{<i})$ and the phase $\phi(\mathbf{x}) := \text{Arg} \sum_{\alpha} \prod_{i=1}^n \tilde{\psi}^{\alpha_{i-1}\alpha_i}(x_i|\mathbf{x}_{<i})$. In other words, we define the amplitude of the wavefunction through the conditional probability distributions and define the phase analogous to the standard MPS.

We develop two different constructions for ANTN that differ in the last layer on how to construct conditional wavefunction tensors.

The elementwise ANTN is given by

$$\tilde{\psi}^{\alpha_{i-1}\alpha_i}(x_i|\mathbf{x}_{<i}) = M_{x_i}^{\alpha_{i-1}\alpha_i} + f_{NN}(x_i, \alpha_{i-1}, \alpha_i|\mathbf{x}_{<i}), \quad (6)$$

where $f_{NN}(x_i, \alpha_{i-1}, \alpha_i|\mathbf{x}_{<i})$ is the complex-valued output. The blockwise ANTN is given by

$$\tilde{\psi}^{\alpha_{i-1}\alpha_i}(x_i|\mathbf{x}_{<i}) = M_{x_i}^{\alpha_{i-1}\alpha_i} + f_{NN}(x_i|\mathbf{x}_{<i}), \quad (7)$$

where the complex-valued output $f_{NN}(x_i|\mathbf{x}_{<i})$ is broadcasted over α . This results in a lower complexity that allows us to use a larger maximum bond dimension.

Transformer and PixelCNN Based ANTN. Our construction above is general and can be applied to any standard ARNN. Depending on the application, we can use different ARNN architectures. In this work, we choose the transformer and PixelCNN depending on the specific tasks. The transformer (Vaswani et al., 2017) used here is similar to a decoder-only transformer implemented in (Luo et al., 2020), and The PixelCNN we use is the gated PixelCNN (Van den Oord et al., 2016) implemented in (Chen et al., 2022).

MPS Initialization. Since our ANTN generalizes from TN, both the elementwise and the blockwise can take advantage of the optimized MPS from algorithms such as DMRG (White, 1992) as an initialization. In practice, we can initialize the TN component with the optimized DMRG results of the same bond dimension (similar to (Lami et al., 2022; Wu et al., 2022)). The MPS Initialization can also be thought of as a pretraining of the ANTN. This is a nice feature since it provides a good sign structure and inductive bias from physics structure, which does not exist in the conventional ARNN.

Limitations. In this work, we only integrated MPS to the ANTN, where MPS may not be the best TN in various settings. Besides MPS, many other TNs also allow efficient evaluation of conditional probabilities and exact sampling, such as MERA (Vidal, 2007) and PEPS (Verstraete & Cirac, 2004), or cylindrical MPS for periodic boundary conditions. In fact the recently developed TensorRNN (Wu et al., 2022) can also be viewed as a type of TN and can be integrated in our construction for future work. In addition, while the ANTN construction is general in terms of the base ARNN used, our current study only focuses on transformer and PixelCNN. Lastly, as shown later in Sec. 5.1, the current implementation of ANTN has an additional sampling overhead that is linear in system size which can be avoided.

5 Theoretical Results

5.1 Exact Sampling and Complexity Analysis of ANTN

Theorem 5.1. *Autoregressive Neural TensorNet wavefunction is automatically normalized and allows for exact sampling.*

Proof. This is a direct consequence that we defined the amplitude of the wavefunction through normalized conditional probability distributions $q(x_i|\mathbf{x}_{<i})$. (See Appendix B.1 for detailed sampling procedure.) \square

Complexity Analysis. We first note that for MPS, the number of parameters and computational complexity for evaluating a bitstring \mathbf{x} scales as $\mathcal{O}(n\chi^2)$, where n is the number of particles and $\chi = \mathcal{D}(\alpha)$ is the (maximum) bond dimension of MPS. The sampling complexity scales as $\mathcal{O}(n^2\chi^2)$. The DMRG algorithm has a computational complexity of $\mathcal{O}(n\chi^3)$ (White, 1992). The number of parameters and computational complexity of ARNN depends on the specific choice. Assuming the ARNN has n_{ARNN} parameters and a single pass (evaluation) of the ARNN has a computational complexity of c_{ARNN} , then the sampling complexity of the ARNN is $\mathcal{O}(nc_{\text{ARNN}})$ in our current implementation. The ANTN based on such ARNN would have $\mathcal{O}(n_{\text{ARNN}} + n\chi^2h_{\text{dim}})$ parameters for the elementwise construction, and $\mathcal{O}(n_{\text{ARNN}} + n\chi^2 + nh_{\text{dim}})$ parameters for the blockwise construction. The computational complexity for evaluating and sampling bitstrings scales as $\mathcal{O}(n^\gamma(c_{\text{ARNN}} + n\chi^2h_{\text{dim}}))$ for elementwise construction and $\mathcal{O}(n^\gamma(c_{\text{ARNN}} + n\chi^2))$ for blockwise construction with $\gamma = 0$ for evaluation and $\gamma = 1$ for sampling.

We note that the complexity analysis above is based on our current implementation, where the sampling procedure for all algorithms has an $\mathcal{O}(n)$ overhead compared to evaluation. It is possible to remove it by storing the partial results during sampling procedure.

Then, each gradient update of the variational Monte Carlo algorithm requires sampling once and evaluating N_c times where N_c is the number of non-zero \mathbf{x}' 's in $\mathcal{H}_{\mathbf{x}, \mathbf{x}'}$ given \mathbf{x} , which usually scales linearly with the system size. Then, the overall complexity is $\mathcal{O}(N_s(N_c c_{\text{eva}} + c_{\text{samp}}))$ with N_s the batch size, c_{eva} the evaluation cost and c_{samp} the sampling cost. Usually, the first part dominates the cost.

The difference in computational complexities and number of parameters between elementwise ANTN and blockwise ANTN implies that blockwise ANTN is usually more economical than elementwise ANTN for the same h_{dim} and χ . Therefore, for small bond dimension, we use the elementwise ANTN for a more flexible parameterization with a higher cost. In contrast, for large bond dimension we use the blockwise ANTN, which saves computational complexity and improves the initial performance (with DMRG initialization) of the blockwise ANTN at the cost of less flexible modifications from the ARNN. We also note that compared to the state-of-the-arts MPS simulation, even for our blockwise ANTN, a small bond dimension usually suffices. For example, in the later experimental section, we use bond dimension 70 for blockwise ANTN while the best DMRG results use bond dimension 1024, which has much more parameters than our ANTN. In general, our ANTN has much fewer parameters compared to MPS due to the $\mathcal{O}(\chi^2)$ parameters scaling which dominates at large bond dimension.

5.2 Expressivity Results of ANTN

Theorem 5.2. *Autoregressive Neural TensorNet has generalized expressivity over tensor network and autoregressive neural network.*

Proof. (See detail in Thm B.2 of Appendix B.4.) If we set $\mathcal{D}(\alpha_i) = 1$ for all i , the marginal probability distribution in Eq. 4 reduces to that of the standard ARNN (up to normalization). This means both the conditional and full probability distributions are the same. The phase of the ANTN becomes a sum of the phases of each conditional wavefunction, which also reduces to the ARNN. This shows that ARNN is a special case of ANTN.

If we set $f_{NN}^{\alpha_{i-1}\alpha_i}(x_i|\mathbf{x}_{<i}) = 0$ in Eq. 6 and $f_{NN}(x_i|\mathbf{x}_{<i}) = 0$ in Eq. 7, then ANTN reduces to the TN shown in Eq. 3. This shows that TN is also a special case of ANTN. Thus ANTN generalizes both ARNN and TN with more expressivity. \square

Theorem 5.3. *Autoregressive Neural TensorNet can have volume law entanglement, which is strictly beyond the expressivity of matrix product state.*

Proof. We proved in Thm. 5.2 that ANTN can be reduced to an ARNN, which has been shown to have volume law entanglement that cannot be efficiently represented by TN (Sharir et al., 2021; Levine et al., 2019b). Hence, ANTN can represent states that cannot in general be represented by MPS efficiently; thus it has strictly greater expressivity. \square

5.3 Symmetry Results of ANTN

Symmetry plays an important role in quantum many-body physics and quantum chemistry. Many of the symmetries can be enforced in ARNN via the two classes of the symmetries—*mask symmetry* and *function symmetry*.

Definition 5.1 (Mask Symmetry). A conditional wavefunction $\psi(x_i|\mathbf{x}_{<i})$ has a *mask symmetry* if $\psi(x_i|\mathbf{x}_{<i}) = 0$ for some x_i given $\mathbf{x}_{<i}$.

Definition 5.2 (Function Symmetry). For a function F that satisfies $\{F(x_i), F(\mathbf{x}_{<i})\} = F(\mathbf{x}_{\leq i})$, a conditional wavefunction tensor $\psi(x_i|\mathbf{x}_{<i})$ has a *function symmetry* over the F if $\psi(x_i|\mathbf{x}_{<i}) = \psi(F(x_i)|F(\mathbf{x}_{<i}))$. Here, $F(x_i)$ is allowed to also depend on $\mathbf{x}_{<i}$.

Here, we list several symmetries that ANTN inherits from ARNN and show the proofs in Appendix B.4.

Theorem 5.4. *Autoregressive Neural TensorNet inherits mask symmetry and function symmetry from autoregressive neural networks.*

Corollary 5.4.1 (Global U(1) Symmetry). *Autoregressive Neural TensorNet can realize global U(1) symmetry, which conserves particle number.*

Corollary 5.4.2 (\mathbb{Z}_2 Spin Flip Symmetry). *Autoregressive Neural TensorNet can realize \mathbb{Z}_2 spin flip symmetry such that the wavefunction is invariant under conjugation of the input.*

Corollary 5.4.3 (Discrete Abelian and Non-Abelian Symmetries). *Autoregressive Neural TensorNet can realize discrete Abelian and Non-Abelian symmetries.*

6 Experiments

The details in experiment setup and hyperparameters can be found in Appendix C.

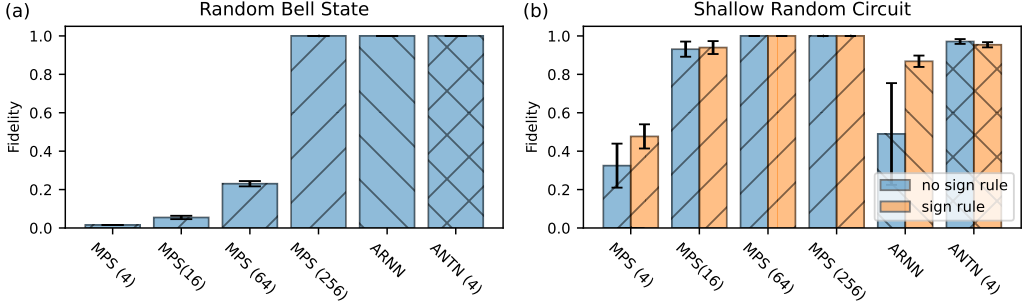


Figure 2: Fidelity \uparrow on quantum state learning with 16 qubits. (a) Learning random Bell states. (b) Learning real-valued depth-4 random circuit with and without sign rule. The error bar denotes the standard deviation (not standard error of mean) of the fidelities over the random states sampled from the corresponding distribution. The mean and standard deviation are calculated from 10 random states. The numbers inside the parentheses denote the bond dimension.

6.1 Quantum State Learning

As stated previous, ANTN generalizes both ARNN and TN to take advantage of both the expressivity and the inductive bias. Here, we test the ANTN on learning physically important quantum states to demonstrate this ability.

Experiments on expressivity. We first test the expressivity of the ANTN by learning a class of well-known high-entangled states—random permuted Bell states. A 2-qubit Bell state is defined as $(|00\rangle + |11\rangle)/\sqrt{2}$, which has 1 bit of entanglement. For a system size of n , we randomly pair qubits in the first half of the system with the qubits in the second half of the system to be Bell states. This process creates quantum states with $n/2$ bit of entanglement between the first and second half of the system. It can be shown that a bond dimension of $2^{n/2}$ is required for MPS to fully represent such a system. In Fig. 2 (a), we plot the quantum fidelity of learning 16-qubit random Bell states. As the figure shows, MPS cannot represent the states without reaching the required bond dimension of $256 = 2^8$. The ARNN and ANTN, on the other hand, can represent such states without limitations from bond dimension.

Experiments on inductive bias. We then test the physics inductive bias of the ANTN. One consequence of the physics inductive bias of MPS is that it can represent wavefunctions with local or quasi-local sign structures that can be hard for neural networks to learn, since these structures usually comes from physical interactions. Here, we use (real-valued) shallow random circuit to mimic the short-range interaction and generate states with sign structures. We test the algorithms on these states both with and without the “sign rule”, which means that we explicitly provide the sign structure to the algorithm. As shown in Fig. 2 (b), the fidelity of MPS only depends weakly on the sign rule, whereas the fidelity of ARNN can change drastically. Our ANTN inherits the property of MPS and is not affected by the sign structure. In fact, the ANTN with a bond dimension of 4 already performs better than MPS with a bond dimension of 16.

6.2 Variational Monte Carlo

We further test our algorithm on finding the ground state of the challenging 2D J_1 - J_2 Heisenberg model with open boundary condition. The model has a rich phase diagram with at least three different phases across different J_2/J_1 values (Capriotti et al., 2004) (Lante & Parola, 2006). In addition, the complicated structure of its ground state makes it a robust model on which to test state-of-the-art methods.

The 2D J_1 - J_2 Hamiltonian is given by

$$\hat{\mathcal{H}} = J_1 \sum_{\langle i,j \rangle} \vec{\sigma}_i \cdot \vec{\sigma}_j + J_2 \sum_{\langle\langle i,j \rangle\rangle} \vec{\sigma}_i \cdot \vec{\sigma}_j, \quad (8)$$

Algorithms	Energy per site $\downarrow 8 \times 8$		
	$J_2 = 0.2$	$J_2 = 0.5$	$J_2 = 0.8$
RBM (NS)	-1.9609(16)	-1.5128(20)	-1.7508(19)
RBM (S)	-2.1944(17)	-1.8625(20)	-0.7267(29)
PixelCNN (NS)	-2.21218(16)	-1.77058(29)	-1.93825(16)
PixelCNN (S)	-2.23171(9)	-1.88902(19)	-1.83672(26)
Elementwise (8 NS)	-2.23690(4)	<i>-1.93018(8)</i>	<i>-2.00036(16)</i>
Elementwise (8 S)	<i>-2.23688(4)</i>	-1.93102(7)	-2.00262(11)
Blockwise (70 NS)	-2.23484(7)	-1.93000(7)	-1.99148(13)
Blockwise (70 S)	-2.23517(6)	-1.92880(9)	-1.99246(13)

Table 1: Energy per site \downarrow for 8×8 system with various algorithms. The bond dimensions for elementwise and blockwise ANTN are labeled inside the parentheses. For each algorithm, we test it both with the sign rule (S) and without the sign rule (NS). The best energy is highlighted in boldface and the second in italic.

Algorithms	Energy per site $\downarrow 10 \times 10$							
	$J_2 = 0.2$	$J_2 = 0.3$	$J_2 = 0.4$	$J_2 = 0.5$	$J_2 = 0.6$	$J_2 = 0.7$	$J_2 = 0.8$	$J_2 = 0.9$
DMRG (8)	-1.997537	-1.893753	-1.797675	-1.734326	-1.716253	-1.768225	-1.869871	
DMRG (70)	-2.191048	-2.069029	-1.956480	-1.866159	-1.816249	-1.854296	-2.007845	
DMRG (1024)	-2.255633	-2.138591	-2.031681	<i>-1.938770</i>	-1.865561	-1.894371	-2.062730	
PixelCNN	-2.22462(24)	-2.12873(14)	-2.02053(14)	-1.74098(29)	-1.71885(27)	-1.81800(13)	-1.98331(17)	
Elementwise (8)	-2.26034(6)	-2.14450(4)	-2.03727(7)	-1.94001(6)	<i>-1.85684(10)</i>	<i>-1.88643(7)</i>	<i>-2.05707(43)</i>	
Blockwise (70)	-2.25755(8)	-2.14152(8)	-2.03319(10)	-1.93842(42)	-1.85270(12)	-1.87853(13)	-2.05088(14)	

Algorithms	Energy per site $\downarrow 12 \times 12$							
	$J_2 = 0.2$	$J_2 = 0.3$	$J_2 = 0.4$	$J_2 = 0.5$	$J_2 = 0.6$	$J_2 = 0.7$	$J_2 = 0.8$	$J_2 = 0.9$
DMRG (8)	-1.998207	-1.887531	-1.800784	-1.735906	-1.720619	-1.788652	-1.893916	
DMRG (70)	-2.185071	-2.059443	-1.944832	-1.851954	-1.812450	-1.853650	-2.030131	
DMRG (1024)	<i>-2.264084</i>	-2.141043	-2.027736	-1.931243	-1.858846	<i>-1.913483</i>	<i>-2.093013</i>	
PixelCNN	-2.24311(102)	-2.12616(23)	-2.01768(21)	-1.74282(30)	-1.72637(16)	-1.85239(13)	-2.03226(59)	
Elementwise (8)	-2.27446(27)	-2.15537(6)	-2.04437(7)	-1.94686(6)	<i>-1.85443(15)</i>	-1.91391(10)	-2.09457(10)	
Blockwise (70)	-2.26152(50)	-2.15395(7)	-2.04225(8)	-1.94298(43)	-1.85176(15)	-1.90571(12)	-2.09113(43)	

Table 2: Energy per site \downarrow for 10×10 and 12×12 system with various algorithms where elementwise and blockwise are two constructions of ANTN. The bond dimensions for DMRG and ANTN are labeled in the parentheses. The best energy is highlighted in boldface and the second best value is highlighted in italic.

where subscript refers to the site of the qubits, $\langle \cdot, \cdot \rangle$ is the nearest neighbour and $\langle\langle \cdot, \cdot \rangle\rangle$ is the next nearest neighbour. $\vec{\sigma}_i \cdot \vec{\sigma}_j = X_i \otimes X_j + Y_i \otimes Y_j + Z_i \otimes Z_j$ with X, Y and Z the Pauli matrices

$$X = \begin{bmatrix} 0 & 1 \\ 1 & 0 \end{bmatrix}, \quad Y = \begin{bmatrix} 0 & -i \\ i & 0 \end{bmatrix}, \quad Z = \begin{bmatrix} 1 & 0 \\ 0 & -1 \end{bmatrix}. \quad (9)$$

We will fix $J_1 = 1$ and vary J_2 in our studies.

Experiments on inductive bias of J_1 - J_2 Heisenberg Model.

As shown previously, it can be challenging for neural networks to learning the sign structures of the J_1 - J_2 model. There is a sign rule for this model known as the Marshall sign rule, which is approximate for $J_2 \neq 0$ (Marshall, 1955). We test the restricted Boltzmann machine (RBM) (from NetKet (Vicentini et al., 2022)), PixelCNN, and the two different constructions of ANTN. The result is shown in Table 1. Both RBM and PixelCNN improved significantly with the application of the sign rule at $J_2 = 0.2$ and $J_2 = 0.5$, but the result deteriorates at $J_2 = 0.8$. This is expected because the sign rule becomes increasingly inaccurate as J_2 increases, especially pass $J_2 = 0.5$. Our ANTN, on the other hand, does not require the sign rule in both constructions. We note that both of our ANTN construction achieved better result compared to the recently developed matrix product backflow state (Lami et al., 2022), which uses the sign rule and has an per site energy of -1.9267 at $J_2 = 0.5$.

Ablation study on J_1 - J_2 Heisenberg Model. We scan across many J_2 for the model without using the sign rule. In this experiment, we compare the performance of six models to compute the ground state energy of the J_1 - J_2 Hamiltonian system with $J_1 = 1$ fixed and $J_2 = 0.2$ - 0.8 with 0.1 increment, covering three different phases of the model. The first three models are TN models, using the DMRG

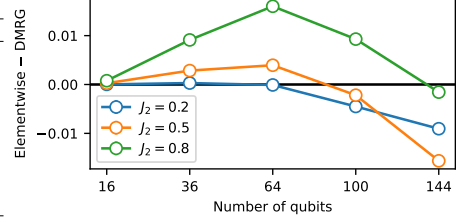


Figure 3: Energy per site difference \downarrow between elementwise ANTN with bond dimension 8 and DMRG with bond dimension 1024 for various J_2 and different system sizes from 4×4 to 12×12 .

algorithm with bond dimensions of 8, 70, and 1024. For up to 20 qubits, the DMRG results with bond dimension 1024 is exact and can be regarded as a benchmark. The fourth model is a PixelCNN pure neural network; the fifth and sixth models are elementwise and blockwise ANTN models. Thus the experiment compares our novel architecture (fifth and sixth models) against the two previous state-of-the-art techniques (first through fourth models).

Since our approach is based on the variational principle discussed in Sec. 3, it provides an upper bound on the exact ground state energy; therefore, a lower energy implies a better state. Table 2 summarizes the per site ground state energy computed by different models at different J_2 ’s in three distinct phases. Our results provide strong evidence that ANTN integrating TN and ARNN outperforms each base model, achieving state-of-the-art results.

Discussion. In all cases the ANTN surpasses the DMRG with the corresponding bond dimension on which they are based. For example, even in the 10×10 system with $J_2 > 0.5$, where DMRG 1024 outperforms the ANTN, the elementwise ANTN still significantly improves on the base DMRG 8 result and the blockwise ANTN improves on the base DMRG 70 result. It is consistent with Theorem. 5.2 and Theorem. 5.3 that ANTN is more expressive than TN. The elementwise and blockwise ANTN models also consistently outperform the pure neural network PixelCNN model. This agrees with Theorem 5.2 that both elementwise and blockwise ANTN have a generalized expressivity compared to ARNN.

In addition, the ANTN models scale well for larger systems. Figure 3 visualizes the scalability of ANTN compared to DMRG. The figure plots the difference in per site energy between the elementwise ANTN with bond dimension 8 and DMRG with bond dimension 1024 for $J_2 = 0.2, 0.5, 0.8$ where lower energies signify better performance for the elementwise ANTN. Compared to DMRG, the ANTN models compute better ground state energies as the system size grows larger. As the system size increases, the elementwise ANTN with bond dimension 8 starts to outperforms DMRG with bond dimension 1024. Even at $J_2 = 0.6$, where the elementwise ANTN is slightly worse than DMRG, the difference gets significantly smaller at 12×12 compared to 10×10 (Table 2). In fact, the elementwise ANTN achieves such a performance using only $\sim 1\%$ the number of parameters of DMRG.

The DMRG has a cost dominated by the bond dimension (quadratic for memory and cubic for computational), which limits its use in practice for large system sizes which can require large bond dimensions. According to the complexity analysis in Sec. 5.1, ANTN has lower complexity than TN and thus scales better for larger systems. We note that for large J_2 , the system goes into a stripped phase (Nomura & Imada, 2021), which can be less challenging for DMRG calculation. Nevertheless, in almost all cases our ANTN still outperforms DMRG on the 12×12 system.

7 Conclusion

In this paper, we developed Autoregressive Neural TensorNet, bridging the two state-of-the-art methods in the field, tensor networks and autoregressive neural networks. We proved that Autoregressive Neural TensorNet is self-normalized with exact sampling, naturally generalizes the expressivity of both tensor networks and autoregressive neural networks, and inherits proper physics inductive bias from tensor networks and various symmetries from autoregressive neural networks. We demonstrated our approach on quantum state learning and the challenging 2D J_1 - J_2 Heisenberg model with different system sizes and couplings. Our results achieve better performance than both the original tensor network and autoregressive neural network while surpassing tensor networks with large bond dimension as the system size increases. Besides scientific applications, since both tensor networks and autoregressive neural networks have been applied to machine learning tasks such as supervised learning and generative modeling, Autoregressive Neural TensorNet can also be applied to these other contexts. Our novel approach holds promise for better performance in these other domains due to its exact sampling, expressivity, and symmetries.

Broader Impact. Our Autoregressive Neural TensorNet, blending tensor networks and autoregressive neural networks, could advance our grasp of quantum phenomena, potentially fueling scientific breakthroughs. It enhances quantum material design and quantum computing through improved simulations and control of quantum states. This technology may also inspire new machine learning models for handling high-dimensional data. However, possible ethical and societal impacts, such as the use for chemical weapon development, require careful scrutiny.

References

Barrett, T. D., Malyshev, A., and Lvovsky, A. Autoregressive neural-network wavefunctions for ab initio quantum chemistry. *Nature Machine Intelligence*, 4(4):351–358, 2022.

Capriotti, L., Fubini, A., Roscilde, T., and Tognetti, V. Ising transition in the two-dimensional quantum j_1 - j_2 heisenberg model. *Physical review letters*, 92(15):157202, 2004.

Carleo, G. and Troyer, M. Solving the quantum many-body problem with artificial neural networks. *Science*, 355(6325):602–606, 2017. doi: 10.1126/science.aag2302. URL <https://www.science.org/doi/10.1126/science.aag2302>.

Chen, Z., Luo, D., Hu, K., and Clark, B. K. Simulating 2+ 1d lattice quantum electrodynamics at finite density with neural flow wavefunctions. *arXiv preprint arXiv:2212.06835*, 2022.

Choo, K., Neupert, T., and Carleo, G. Two-dimensional frustrated J_1 - J_2 model studied with neural network quantum states. *Phys. Rev. B*, 100:125124, Sep 2019. doi: 10.1103/PhysRevB.100.125124. URL <https://link.aps.org/doi/10.1103/PhysRevB.100.125124>.

Deng, D.-L., Li, X., and Das Sarma, S. Quantum entanglement in neural network states. *Physical Review X*, 7(2), May 2017. ISSN 2160-3308. doi: 10.1103/physrevx.7.021021. URL <http://dx.doi.org/10.1103/PhysRevX.7.021021>.

Ferris, A. J. and Vidal, G. Perfect sampling with unitary tensor networks. *Phys. Rev. B*, 85:165146, Apr 2012. doi: 10.1103/PhysRevB.85.165146. URL <https://link.aps.org/doi/10.1103/PhysRevB.85.165146>.

Gao, X. and Duan, L.-M. Efficient representation of quantum many-body states with deep neural networks. *Nature Communications*, 8(1):662, Sep 2017. ISSN 2041-1723. doi: 10.1038/s41467-017-00705-2. URL <https://www.nature.com/articles/s41467-017-00705-2>.

Girvin, S. M. and Yang, K. *Modern condensed matter physics*. Cambridge University Press, 2019.

Greensmith, E., Bartlett, P. L., and Baxter, J. Variance reduction techniques for gradient estimates in reinforcement learning. *J. Mach. Learn. Res.*, 5:1471–1530, December 2004. ISSN 1532-4435.

Gutiérrez, I. L. and Mendl, C. B. Real time evolution with neural-network quantum states, 2020.

Hartmann, M. J. and Carleo, G. Neural-network approach to dissipative quantum many-body dynamics. *Phys. Rev. Lett.*, 122:250502, Jun 2019. doi: 10.1103/PhysRevLett.122.250502. URL <https://journals.aps.org/prl/abstract/10.1103/PhysRevLett.122.250502>.

Hermann, J., Schätzle, Z., and Noé, F. Deep neural network solution of the electronic schrödinger equation, 2019.

Hibat-Allah, M., Ganahl, M., Hayward, L. E., Melko, R. G., and Carrasquilla, J. Recurrent neural network wave functions. *Phys. Rev. Research*, 2:023358, Jun 2020. doi: 10.1103/PhysRevResearch.2.023358. URL <https://journals.aps.org/prresearch/abstract/10.1103/PhysRevResearch.2.023358>.

Huang, Y. and Moore, J. E. Neural network representation of tensor network and chiral states. *Phys. Rev. Lett.*, 127:170601, Oct 2021. doi: 10.1103/PhysRevLett.127.170601. URL <https://link.aps.org/doi/10.1103/PhysRevLett.127.170601>.

Lami, G., Carleo, G., and Collura, M. Matrix product states with backflow correlations. *Physical Review B*, 106(8), aug 2022. doi: 10.1103/physrevb.106.108111. URL <https://doi.org/10.1103%2Fphysrevb.106.108111>.

Lante, V. and Parola, A. The ising phase in the j_1 - j_2 heisenberg model. *Physical Review*, 2006.

Levine, Y., Sharir, O., Cohen, N., and Shashua, A. Quantum entanglement in deep learning architectures. *Physical Review Letters*, 122(6), Feb 2019a. ISSN 1079-7114. doi: 10.1103/physrevlett.122.065301. URL <https://journals.aps.org/prl/abstract/10.1103/PhysRevLett.122.065301>.

Levine, Y., Sharir, O., Cohen, N., and Shashua, A. Quantum entanglement in deep learning architectures. *Physical review letters*, 122(6):065301, 2019b.

Lu, S., Gao, X., and Duan, L.-M. Efficient representation of topologically ordered states with restricted boltzmann machines. *Phys. Rev. B*, 99:155136, Apr 2019. doi: 10.1103/PhysRevB.99.155136. URL <https://journals.aps.org/prb/abstract/10.1103/PhysRevB.99.155136>.

Luo, D. and Clark, B. K. Backflow transformations via neural networks for quantum many-body wave functions. *Physical Review Letters*, 122(22), Jun 2019. ISSN 1079-7114. doi: 10.1103/physrevlett.122.226401. URL <https://journals.aps.org/prl/abstract/10.1103/PhysRevLett.122.226401>.

Luo, D., Chen, Z., Carrasquilla, J., and Clark, B. K. Autoregressive neural network for simulating open quantum systems via a probabilistic formulation, 2020.

Luo, D., Carleo, G., Clark, B. K., and Stokes, J. Gauge equivariant neural networks for quantum lattice gauge theories. *Physical review letters*, 127(27):276402, 2021a.

Luo, D., Chen, Z., Hu, K., Zhao, Z., Hur, V. M., and Clark, B. K. Gauge invariant autoregressive neural networks for quantum lattice models, 2021b. URL <https://arxiv.org/abs/2101.07243>.

Luo, D., Chen, Z., Carrasquilla, J., and Clark, B. K. Autoregressive neural network for simulating open quantum systems via a probabilistic formulation. *Phys. Rev. Lett.*, 128:090501, Feb 2022a. doi: 10.1103/PhysRevLett.128.090501. URL <https://link.aps.org/doi/10.1103/PhysRevLett.128.090501>.

Luo, D., Yuan, S., Stokes, J., and Clark, B. K. Gauge equivariant neural networks for 2+ 1d u (1) gauge theory simulations in hamiltonian formulation. *arXiv preprint arXiv:2211.03198*, 2022b.

Marshall, W. Antiferromagnetism. *Proceedings of the Royal Society of London. Series A, Mathematical and Physical Sciences*, 232(1188):48–68, 1955. ISSN 00804630. URL <http://www.jstor.org/stable/99682>.

Nagy, A. and Savona, V. Variational quantum monte carlo method with a neural-network ansatz for open quantum systems. *Phys. Rev. Lett.*, 122:250501, Jun 2019. doi: 10.1103/PhysRevLett.122.250501. URL <https://journals.aps.org/prl/abstract/10.1103/PhysRevLett.122.250501>.

Nomura, Y. and Imada, M. Dirac-type nodal spin liquid revealed by refined quantum many-body solver using neural-network wave function, correlation ratio, and level spectroscopy. *Physical Review X*, 11(3), aug 2021. doi: 10.1103/physrevx.11.031034. URL <https://doi.org/10.1103%2Fphysrevx.11.031034>.

Oseledets, I. V. Tensor-train decomposition. *SIAM Journal on Scientific Computing*, 33(5):2295–2317, 2011. doi: 10.1137/090752286. URL <https://doi.org/10.1137/090752286>.

Paszke, A., Gross, S., Massa, F., Lerer, A., Bradbury, J., Chanan, G., Killeen, T., Lin, Z., Gimelshein, N., Antiga, L., et al. Pytorch: An imperative style, high-performance deep learning library. In *Advances in neural information processing systems*, pp. 8026–8037, 2019.

Pfau, D., Spencer, J. S., Matthews, A. G. D. G., and Foulkes, W. M. C. Ab initio solution of the many-electron schrödinger equation with deep neural networks. *Phys. Rev. Research*, 2:033429, Sep 2020. doi: 10.1103/PhysRevResearch.2.033429. URL <https://journals.aps.org/prresearch/abstract/10.1103/PhysRevResearch.2.033429>.

Preskill, J. Quantum computing 40 years later. *arXiv preprint arXiv:2106.10522*, 2021.

Schmitt, M. and Heyl, M. Quantum many-body dynamics in two dimensions with artificial neural networks. *Physical Review Letters*, 125(10), Sep 2020. ISSN 1079-7114. doi: 10.1103/physrevlett.125.100503. URL <https://journals.aps.org/prl/abstract/10.1103/PhysRevLett.125.100503>.

Sharir, O., Levine, Y., Wies, N., Carleo, G., and Shashua, A. Deep autoregressive models for the efficient variational simulation of many-body quantum systems. *Physical Review Letters*, 124(2), jan 2020. doi: 10.1103/physrevlett.124.020503. URL <https://doi.org/10.1103/2Fphysrevlett.124.020503>.

Sharir, O., Shashua, A., and Carleo, G. Neural tensor contractions and the expressive power of deep neural quantum states, 2021.

Van den Oord, A., Kalchbrenner, N., Espeholt, L., Vinyals, O., Graves, A., et al. Conditional image generation with pixelcnn decoders. *Advances in neural information processing systems*, 29, 2016.

Vaswani, A., Shazeer, N., Parmar, N., Uszkoreit, J., Jones, L., Gomez, A. N., Kaiser, Ł., and Polosukhin, I. Attention is all you need. *Advances in neural information processing systems*, 30: 5998–6008, 2017.

Verstraete, F. and Cirac, J. I. Renormalization algorithms for quantum-many body systems in two and higher dimensions, 2004. URL <https://arxiv.org/abs/cond-mat/0407066>.

Vicentini, F., Biella, A., Regnault, N., and Ciuti, C. Variational neural-network ansatz for steady states in open quantum systems. *Physical Review Letters*, 122(25), Jun 2019. ISSN 1079-7114. doi: 10.1103/physrevlett.122.250503. URL <https://journals.aps.org/prl/abstract/10.1103/PhysRevLett.122.250503>.

Vicentini, F., Hofmann, D., Szabó, A., Wu, D., Roth, C., Giuliani, C., Pescia, G., Nys, J., Vargas-Calderón, V., Astrakhantsev, N., and Carleo, G. NetKet 3: Machine learning toolbox for many-body quantum systems. *SciPost Physics Codebases*, aug 2022. doi: 10.21468/scipostphyscodeb.7. URL <https://doi.org/10.21468%2Fscipostphyscodeb.7>.

Vidal, G. Efficient classical simulation of slightly entangled quantum computations. *Physical Review Letters*, 91(14), oct 2003. doi: 10.1103/physrevlett.91.147902. URL <https://doi.org/10.1103%2Fphysrevlett.91.147902>.

Vidal, G. Efficient simulation of one-dimensional quantum many-body systems. *Physical Review Letters*, 93(4), jul 2004. doi: 10.1103/physrevlett.93.040502. URL <https://doi.org/10.1103%2Fphysrevlett.93.040502>.

Vidal, G. Entanglement renormalization. *Phys. Rev. Lett.*, 99:220405, Nov 2007. doi: 10.1103/PhysRevLett.99.220405. URL <https://link.aps.org/doi/10.1103/PhysRevLett.99.220405>.

Viejra, T., Casert, C., Nys, J., De Neve, W., Haegeman, J., Ryckebusch, J., and Verstraete, F. Restricted boltzmann machines for quantum states with non-abelian or anyonic symmetries. *Physical Review Letters*, 124(9), Mar 2020. ISSN 1079-7114. doi: 10.1103/physrevlett.124.097201. URL <https://journals.aps.org/prl/abstract/10.1103/PhysRevLett.124.097201>.

Westerhout, T., Astrakhantsev, N., Tikhonov, K. S., Katsnelson, M. I., and Bagrov, A. A. Generalization properties of neural network approximations to frustrated magnet ground states. *Nature Communications*, 11(1):1593, Mar 2020. ISSN 2041-1723. doi: 10.1038/s41467-020-15402-w. URL <https://doi.org/10.1038/s41467-020-15402-w>.

White, S. R. Density matrix formulation for quantum renormalization groups. *Physical review letters*, 69(19):2863, 1992.

Wu, D., Rossi, R., Vicentini, F., and Carleo, G. From tensor network quantum states to tensorial recurrent neural networks. *arXiv preprint arXiv:2206.12363*, 2022.

Yoshioka, N. and Hamazaki, R. Constructing neural stationary states for open quantum many-body systems. *Phys. Rev. B*, 99:214306, Jun 2019. doi: 10.1103/PhysRevB.99.214306. URL <https://journals.aps.org/prb/abstract/10.1103/PhysRevB.99.214306>.

Appendices

A Additional Background

A.1 Quantum State Learning

In this section, we discuss more details about quantum state learning. As mentioned in the main paper, the quantum fidelity

$$F = |\langle \phi | \psi_\theta \rangle|^2 = \left| \sum_{\mathbf{x}} \phi^*(\mathbf{x}) \psi_\theta(\mathbf{x}) \right|^2 \quad (\text{A.1})$$

measures the closeness of the two (normalized) quantum states $|\phi\rangle$ and $|\psi_\theta\rangle$, with $*$ denotes complex conjugation. By minimizing $-\log F$, one can obtain the $|\psi_\theta\rangle$ closest to the target state $|\phi\rangle$ (see Appendix C for optimization details). For small system sizes ($\lesssim 20$ qubits), it is possible to enumerate all the basis \mathbf{x} and compute $-\log F$ exactly as in the case of this work. As mentioned in the main paper, we learn the random Bell state and shallow random circuit to test the expressivity and physics inductive bias of the ansatz. More specifically, the states are generated as follows

Random Bell State. A two-qubit Bell state is defined to be the state $(|00\rangle + |11\rangle)/\sqrt{2}$. We use the following algorithm to generate a n -qubit random Bell state (n is a multiple of 2).

Algorithm 1 Random Bell State Generation

```

 $a \leftarrow \text{shuffle}([1, \dots, \frac{n}{2}])$ 
 $b \leftarrow \text{shuffle}([\frac{n}{2} + 1, \dots, n])$ 
 $\Psi \leftarrow []$ 
 $i \leftarrow 1$ 
while  $i \leq n/2$  do
     $\Psi.\text{append}(\text{bell\_state}(a_i, b_i))$ 
     $i \leftarrow i + 1$ 
end while
 $|\psi\rangle \leftarrow \text{product\_state}(\Psi)$ 
return  $|\psi\rangle$ 

```

where $\text{bell_state}(\cdot, \cdot)$ creates a Bell state given the two qubits and $\text{product_state}([])$ creates the tensor product state for a list of individual states. Each two-qubit Bell state in the random Bell state forms between the left half and right half of the system, allowing a maximum entanglement across a cut in the middle of the system.

Shallow Random Circuit. The shallow random circuit generates random states using the following algorithm.

Algorithm 2 Shallow Random Circuit State Generation

```

 $|\psi\rangle \leftarrow |0\rangle^{\otimes n}$ 
 $l \leftarrow 1$ 
while  $l \leq n_l$  do
   $i \leftarrow 1$ 
  while  $i < n$  do
     $U \leftarrow \text{random\_gate}(i, i + 1)$ 
     $|\psi\rangle \leftarrow U |\psi\rangle$ 
     $i \leftarrow i + 2$ 
  end while
   $i \leftarrow 2$ 
  while  $i < n$  do
     $U \leftarrow \text{random\_gate}(i, i + 1)$ 
     $|\psi\rangle \leftarrow U |\psi\rangle$ 
     $i \leftarrow i + 2$ 
  end while
end while
return  $|\psi\rangle$ 

```

where n_l is the number of layers, and $\text{random_gate}(\cdot, \cdot)$ generates a random unitary gate on the two qubits. The $\text{random_gate}(\cdot, \cdot)$ function is realized by first generating a (real-valued) Gaussian random matrix of size 4×4 , following a QR decomposition of the matrix to obtain the unitary part as the random unitary gate.

Each of the above algorithm defines a distribution of states, which we average over multiple realizations to compute the mean and standard deviation of the learned quantum fidelity.

A.2 Variational Monte Carlo

As shown in the main paper, given a Hamiltonian $\hat{\mathcal{H}}$ (and its matrix elements $\mathcal{H}_{\mathbf{x}, \mathbf{x}'}$)

$$\langle \psi_\theta | \hat{\mathcal{H}} | \psi_\theta \rangle = \sum_{\mathbf{x}, \mathbf{x}'} \mathcal{H}_{\mathbf{x}, \mathbf{x}'} \psi_\theta^*(\mathbf{x}) \psi_\theta(\mathbf{x}') = \sum_{\mathbf{x}, \mathbf{x}'} |\psi_\theta(\mathbf{x})|^2 \frac{\mathcal{H}_{\mathbf{x}, \mathbf{x}'} \psi_\theta(\mathbf{x}')}{\psi_\theta(\mathbf{x})} = \mathbb{E}_{\mathbf{x} \sim |\psi_\theta|^2} \frac{\sum_{\mathbf{x}'} \mathcal{H}_{\mathbf{x}, \mathbf{x}'} \psi_\theta(\mathbf{x}')}{\psi_\theta(\mathbf{x})}. \quad (\text{A.2})$$

Since the Hamiltonian $\hat{\mathcal{H}}$ is usually sparse, give \mathbf{x} , one only needs to sum up a small number of \mathbf{x}' 's for the numerator (usually linear in system size), allowing Eq. A.2 to be evaluated efficiently. Analogously, we can evaluate the gradient as

$$\begin{aligned} \nabla_\theta \langle \psi_\theta | \hat{\mathcal{H}} | \psi_\theta \rangle &= 2\Re \sum_{\mathbf{x}, \mathbf{x}'} \mathcal{H}_{\mathbf{x}, \mathbf{x}'} [\nabla_\theta \psi_\theta^*(\mathbf{x})] \psi_\theta(\mathbf{x}') \\ &= 2\Re \sum_{\mathbf{x}, \mathbf{x}'} |\psi_\theta(\mathbf{x})|^2 \mathcal{H}_{\mathbf{x}, \mathbf{x}'} \frac{\nabla_\theta \psi_\theta^*(\mathbf{x})}{\psi_\theta^*(\mathbf{x})} \frac{\psi_\theta(\mathbf{x}')}{\psi_\theta(\mathbf{x})} \\ &= 2\Re \mathbb{E}_{\mathbf{x} \sim |\psi_\theta|^2} \frac{\sum_{\mathbf{x}'} \mathcal{H}_{\mathbf{x}, \mathbf{x}'} \psi_\theta(\mathbf{x}')}{\psi_\theta(\mathbf{x})} \nabla_\theta \log \psi_\theta^*(\mathbf{x}). \end{aligned} \quad (\text{A.3})$$

Furthermore, it is possible to reduce the variance by either directly applying the variance reduction formula (Greensmith et al., 2004), or explicitly normalizing $|\psi_\theta\rangle$ (minimizing $\langle \psi_\theta | \hat{\mathcal{H}} | \psi_\theta \rangle / \langle \psi_\theta | \psi_\theta \rangle$) to obtain

$$\nabla_\theta \langle \psi_\theta | \hat{\mathcal{H}} | \psi_\theta \rangle = 2\Re \mathbb{E}_{\mathbf{x} \sim |\psi_\theta|^2} \left[\frac{\sum_{\mathbf{x}'} \mathcal{H}_{\mathbf{x}, \mathbf{x}'} \psi_\theta(\mathbf{x}')}{\psi_\theta(\mathbf{x})} - \langle \psi_\theta | \hat{\mathcal{H}} | \psi_\theta \rangle \right] \nabla_\theta \log \psi_\theta^*(\mathbf{x}), \quad (\text{A.4})$$

where $\langle \psi_\theta | \hat{\mathcal{H}} | \psi_\theta \rangle$ can be approximated by applying Eq. A.2 on the same batch \mathbf{x} . In this work, we use Eq. A.4 as the gradient of the loss function (see Appendix C for optimization details).

B Additional Theoretical Results

B.1 Exact Sampling from Conditional Probabilities

Suppose a full probability distribution over multiple qubits is written as a product of conditional probabilities as

$$p(\mathbf{x}) = p(x_1, \dots, x_n) = \prod_{i=1}^n p(x_i | \mathbf{x}_{<i}) \quad (\text{B.1})$$

with $\mathbf{x}_{<i} = (x_1, \dots, x_{i-1})$, then sampling a bitstring \mathbf{x} from the probability distribution can be obtained by sequentially sampling each conditional probability as Since each sample is sampled

Algorithm 3 Exact Sampling from Conditional Probabilities/Wavefunctions

```

 $\mathbf{x} \leftarrow []$ 
 $i \leftarrow 1$ 
while  $i \leq n$  do
     $\mathbf{x}_{<i} \leftarrow \mathbf{x}$ 
     $x_i \sim p(x_i | \mathbf{x}_{<i})$ 
     $\mathbf{x}.\text{append}(x_i)$ 
     $i \leftarrow i + 1$ 
end while
return  $\mathbf{x}$ 

```

independently using this algorithm, a batch of samples can be obtained in parallel, allowing for an efficient implementation on GPUs. In addition, the exact sampling nature of the algorithm makes it not suffer from the autocorrelation time problem of standard Markov chain Monte Carlo.

This same algorithm applies to sampling from $|\psi(\mathbf{x})|^2$ with a simple replacement $p(x_i | \mathbf{x}_{<i}) \rightarrow |\psi(x_i | \mathbf{x}_{<i})|^2$. This is a direct consequence of

$$\psi(\mathbf{x}) = \prod_{i=1}^n \psi(x_i | \mathbf{x}_{<i}) \Rightarrow |\psi(\mathbf{x})|^2 = \prod_{i=1}^n |\psi(x_i | \mathbf{x}_{<i})|^2, \quad (\text{B.2})$$

and the fact that we require $\sum_{x_i} |\psi(x_i | \mathbf{x}_{<i})|^2 = 1$.

B.2 Exact Sampling from MPS

As mentioned in the main text, matrix product state (MPS) with particular constraint, also allows for exact sampling. Recall that MPS defines a wavefunction as

$$\psi(\mathbf{x}) = \sum_{\alpha_1, \dots, \alpha_{n-1}} M_{x_1}^{\alpha_0 \alpha_1} \cdots M_{x_n}^{\alpha_{n-1} \alpha_n} = \sum_{\alpha} \prod_{i=1}^n M_{x_i}^{\alpha_{i-1} \alpha_i}. \quad (\text{B.3})$$

Let's first assume that the wavefunction is normalized. It is easy to notice that any gauge transformation

$$(M_{x_i}, M_{x_{i+1}}) \rightarrow (M_{x_i} A, A^{-1} M_{x_{i+1}}), \quad (\text{B.4})$$

with A being any invertible matrix does not leaves the resulting wavefunction invariant. Here, we suppress the α indices and view them as the indices for matrices. It has been shown that by fixing this gauge redundancy (Vidal, 2003, 2004), we can restrict all the M matrices to satisfy the following condition

$$\sum_{x_i, \alpha_i} M_{x_i}^{\alpha_{i-1} \alpha_i} \left(M_{x_i}^{\alpha'_{i-1} \alpha_i} \right)^* = \delta_{\alpha_{i-1}, \alpha'_{i-1}}, \quad (\text{B.5})$$

where $\delta_{\cdot, \cdot}$ is the Kronecker delta function. The matrices M that satisfies this condition is called isometries, and the MPS is called in the right canonical form (to be distinguished from the left canonical form). In the right canonical form, each $M_{x_i}^{\alpha_{i-1} \alpha_i}$ can be interpreted as a basis transformation $(x_i, \alpha_i) \rightarrow \alpha_{i-1}$ that is part of a unitary matrix.

Theorem B.1. *Defining the left partially contracted tensors*

$$M_{L\mathbf{x}_{\leq j}}^{\alpha_j} := \sum_{\alpha_{\leq j}} \prod_{i=1}^j M_{x_i}^{\alpha_{i-1}\alpha_i}, \quad (\text{B.6})$$

If the matrix product state is in the right canonical form, then the marginal probability of the wavefunction satisfies

$$q(\mathbf{x}_{\leq i}) := \sum_{\mathbf{x}_{>i}} |\psi(\mathbf{x})|^2 = \sum_{\alpha_j} M_{L\mathbf{x}_{\leq j}}^{\alpha_j} \left(M_{L\mathbf{x}_{\leq j}}^{\alpha_j} \right)^*. \quad (\text{B.7})$$

Proof. Lets define the right partially contracted tensors analogously

$$M_{R\mathbf{x}_{\geq j}}^{\alpha_{j-1}} := \sum_{\alpha_{\geq j}} \prod_{i=j}^n M_{x_i}^{\alpha_{i-1}\alpha_i}. \quad (\text{B.8})$$

We will first show that

$$\sum_{\mathbf{x}_{\geq j}} M_{R\mathbf{x}_{\geq j}}^{\alpha_{j-1}} \left(M_{R\mathbf{x}_{\geq j}}^{\alpha_{j-1}} \right)^* = \delta_{\alpha_{j-1}, \alpha'_{j-1}}. \quad (\text{B.9})$$

We can prove this by induction:

• **Base case:**

$$\sum_{x_n} M_{R\mathbf{x}_n}^{\alpha_{n-1}} \left(M_{R\mathbf{x}_n}^{\alpha_{n-1}} \right)^* = \sum_{x_n} M_{x_n}^{\alpha_{n-1}\alpha_n} \left(M_{x_n}^{\alpha'_{n-1}\alpha'_n} \right)^* = \delta_{\alpha_{n-1}, \alpha'_{n-1}}, \quad (\text{B.10})$$

which directly comes from Eq. B.5 by noticing that $\mathcal{D}(\alpha_n) = 1$ so it can be ignored.

• **Inductive step:** Write

$$M_{R\mathbf{x}_{\geq j}}^{\alpha_{j-1}} = \sum_{\alpha_j} M_{x_j}^{\alpha_{j-1}\alpha_j} M_{R\mathbf{x}_{\geq j+1}}^{\alpha_j}. \quad (\text{B.11})$$

Assuming

$$\sum_{\mathbf{x}_{\geq j+1}} M_{R\mathbf{x}_{\geq j+1}}^{\alpha_j} \left(M_{R\mathbf{x}_{\geq j+1}}^{\alpha'_j} \right)^* = \delta_{\alpha_j, \alpha'_j}, \quad (\text{B.12})$$

then

$$\begin{aligned} \sum_{\mathbf{x}_{\geq j}} M_{R\mathbf{x}_{\geq j}}^{\alpha_{j-1}} \left(M_{R\mathbf{x}_{\geq j}}^{\alpha'_{j-1}} \right)^* &= \sum_{x_j} \sum_{\alpha_j, \alpha'_j} M_{x_j}^{\alpha_{j-1}\alpha_j} \left(M_{x_j}^{\alpha'_{j-1}\alpha'_j} \right)^* \sum_{\mathbf{x}_{\geq j+1}} M_{R\mathbf{x}_{\geq j+1}}^{\alpha_j} \left(M_{R\mathbf{x}_{\geq j+1}}^{\alpha'_j} \right)^* \\ &= \sum_{x_j} \sum_{\alpha_j, \alpha'_j} M_{x_j}^{\alpha_{j-1}\alpha_j} \left(M_{x_j}^{\alpha'_{j-1}\alpha'_j} \right)^* \delta_{\alpha_j, \alpha'_j} \\ &= \sum_{x_j, \alpha_j} M_{x_j}^{\alpha_{j-1}\alpha_j} \left(M_{x_j}^{\alpha'_{j-1}\alpha_j} \right)^* \\ &= \delta_{\alpha_{j-1}, \alpha'_{j-1}}. \end{aligned} \quad (\text{B.13})$$

Using this result, we can then prove our desired result about the marginal probability. Lets write

$$\psi(\mathbf{x}) = \sum_{\alpha} \prod_{i=1}^n M_{x_i}^{\alpha_{i-1}\alpha_i} = \sum_{\alpha_j} M_{L\mathbf{x}_{\leq j}}^{\alpha_j} M_{R\mathbf{x}_{>j}}^{\alpha_j}, \quad (\text{B.14})$$

then,

$$\begin{aligned} q(\mathbf{x}_{\leq i}) &= \sum_{\mathbf{x}_{>i}} |\psi(\mathbf{x})|^2 = \sum_{\mathbf{x}_{>i}} \sum_{\alpha_j, \alpha'_j} M_{L\mathbf{x}_{\leq j}}^{\alpha_j} M_{R\mathbf{x}_{>j}}^{\alpha_j} \left(M_{L\mathbf{x}_{\leq j}}^{\alpha'_j} M_{R\mathbf{x}_{>j}}^{\alpha'_j} \right)^* \\ &= \sum_{\alpha_j, \alpha'_j} M_{L\mathbf{x}_{\leq j}}^{\alpha_j} \left(M_{L\mathbf{x}_{\leq j}}^{\alpha'_j} \right)^* \delta_{\alpha_j, \alpha'_j} \\ &= \sum_{\alpha_j} M_{L\mathbf{x}_{\leq j}}^{\alpha_j} \left(M_{L\mathbf{x}_{\leq j}}^{\alpha_j} \right)^*. \end{aligned} \quad (\text{B.15})$$

□

Corollary B.1.1. *Matrix product state allows for efficient exact sampling.*

Proof. Thm. B.1 shows that marginal probability distribution $q(\mathbf{x}_{\leq i})$ can be evaluated efficiently. The conditional probability can be evaluated efficiently either as $q(x_i|\mathbf{x}_{<i}) = q(\mathbf{x}_{\leq i})/q(\mathbf{x}_{<i})$ or (equivalently) as an explicitly normalization of the marginal probability distribution $q(x_i|\mathbf{x}_{<i}) = q(\mathbf{x}_{\leq i})/\sum_{x_i} q(\mathbf{x}_{\leq i})$. Then, Algorithm 3 can be used to sample from the full distribution. \square

B.3 Autoregressive Sampling Order

Algorithm 3 samples from conditional probabilities, which requires an ordering of the system to be defined. For 1D systems, we use a linear ordering such that qubit 1 corresponds to the left most qubit, and qubit n corresponds to the right most qubit. This ordering is natural for 1D MPS and transformer, as well as the transformer based ANTN. For 2D systems, we use a snake (zig-zag) ordering. In this ordering, the qubit at the 2D location (i, j) is defined to be the $i \times L_y + j$ th qubit, where L_y is the number of qubits along the second dimension. This ordering is inherently defined from the masked convolution for PixelCNN and PixelCNN based ANTN. The MPS is reshaped to satisfy the same ordering for 2D systems. The same 2D ordering can be generalized to other tensor networks as well.

B.4 Additional Details of Expressivity and Symmetry Results of ANTN

Theorem B.2. *Both tensor networks and autoregressive neural networks are special cases of Autoregressive Neural TensorNet.*

Proof. Recall that the ANTN defines the wavefunction from its amplitude and phase

$$\psi(\mathbf{x}) := \sqrt{q(\mathbf{x})} e^{i\phi(\mathbf{x})}, \quad (\text{B.16})$$

where

$$q(\mathbf{x}) = \prod_{j=1}^n q(x_j|\mathbf{x}_{<j}) \quad (\text{B.17})$$

$$\text{with } q(x_j|\mathbf{x}_{<j}) = \frac{q(\mathbf{x}_{\leq j})}{\sum_{x_j} q(\mathbf{x}_{\leq j})} \quad (\text{B.18})$$

$$q(\mathbf{x}_{\leq j}) := \sum_{\alpha_j} \tilde{\psi}_L^{\alpha_j}(\mathbf{x}_{\leq j}) \tilde{\psi}_L^{\alpha_j}(\mathbf{x}_{\leq j})^* \quad (\text{B.19})$$

$$\tilde{\psi}_L^{\alpha_j}(\mathbf{x}_{\leq j}) := \sum_{\alpha_{<j}} \prod_{i=1}^j \tilde{\psi}^{\alpha_{i-1}, \alpha_i}(x_i|\mathbf{x}_{<i}) \quad (\text{B.20})$$

and

$$\phi(\mathbf{x}) =: \text{Arg} \sum_{\alpha} \prod_{i=1}^n \tilde{\psi}^{\alpha_{i-1}, \alpha_i}(x_i|\mathbf{x}_{<i}). \quad (\text{B.21})$$

- **ANTN reduces to MPS.** If we don't modify the tensors with neural networks, $\tilde{\psi}^{\alpha_{i-1}, \alpha_i}(x_i|\mathbf{x}_{<i})$ reduces to $M_{x_i}^{\alpha_{i-1}, \alpha_i}$ and $\tilde{\psi}_L^{\alpha_j}(\mathbf{x}_{\leq j})$ reduces to $M_L^{\alpha_j}_{\mathbf{x}_{\leq j}}$. It is then straightforward that Eq. B.19 reduces to Eq. B.15 and thus the probability distribution of ANTN reduces to that of MPS. Analogously, Eq. B.21 reduces to the phase of an MPS, and thus ANTN wavefunction reduces to MPS wavefunction.
- **ANTN reduces to ARNN.** If we set all $\mathcal{D}(\alpha) = 1$, then $\tilde{\psi}^{\alpha_{i-1}, \alpha_i}(x_i|\mathbf{x}_{<i})$ reduces to $\psi(x_i|\mathbf{x}_{<i})$ and all the summations over α can be dropped. In this case, $q(\mathbf{x}_{\leq j})$ reduces to $\prod_{i=1}^j |\psi(x_i|\mathbf{x}_{<i})|^2$ and $q(x_j|\mathbf{x}_{<j})$ reduces to $|\psi(x_j|\mathbf{x}_{<j})|^2$, which is the same as the standard ARNN. In addition, the phase $\phi(\mathbf{x})$ reduces to $\text{Arg} \prod_{i=1}^n \psi(x_i|\mathbf{x}_{<i})$ which is also the same as ARNN. Thus, ANTN wavefunction reduces to ARNN wavefunction.

Notice that we only showed one type of TN, i.e. MPS, but the proof can be easily generalized to any TN that allows evaluation of marginal probabilities. \square

Definition B.1 (Mask Symmetry). A conditional wavefunction $\psi(x_i|\mathbf{x}_{<i})$ has a *mask symmetry* if $\psi(x_i|\mathbf{x}_{<i}) = 0$ for some x_i given $\mathbf{x}_{<i}$.

Theorem B.3. *Autoregressive Neural TensorNet inherits mask symmetry from autoregressive neural network.*

Proof. The mask symmetry results in $\psi(\mathbf{x}) = 0$ for certain \mathbf{x} satisfying the condition while preserving the normalization of $\psi(\mathbf{x})$. For ANTN, we can directly set $q(x_i|\mathbf{x}_{<i}) = 0$ for the x_i given $\mathbf{x}_{<i}$. This results in $\psi(\mathbf{x}) = 0$ for the same \mathbf{x} . \square

Corollary B.3.1 (Global U(1) Symmetry). *Autoregressive Neural TensorNet can realize global U(1) symmetry, which conserves particle number.*

Proof. A global U(1) symmetry in a qubit system manifests as a conservation of the number of 0's and number of 1's in \mathbf{x} . Equivalently, $\psi(\mathbf{x}) = 0$ for \mathbf{x} violates such conservation. (Hibat-Allah et al., 2020) has shown that autoregressive neural networks can preserve global U(1) symmetry as a mask symmetry, which ANTN inherits. \square

Definition B.2 (Function Symmetry). For a function F that satisfies $\{F(x_i), F(\mathbf{x}_{<i})\} = F(\mathbf{x}_{\leq i})$, a conditional wavefunction tensor $\psi(x_i|\mathbf{x}_{<i})$ has a *function symmetry* over the F if $\psi(x_i|\mathbf{x}_{<i}) = \psi(F(x_i)|F(\mathbf{x}_{<i}))$. Here, $F(x_i)$ is allowed to also depend on $\mathbf{x}_{<i}$.

Theorem B.4. *Autoregressive Neural TensorNet inherits function symmetry from autoregressive neural networks.*

Proof. We can apply the function symmetry on the left partially contracted tensors instead of the conditional wavefunctions. Here, we show that this produces the desired conditional probabilities and phase. Applying the function symmetry on the left partially contracted tensors results in

$$\tilde{\psi}_L^{\alpha_j}(\mathbf{x}_{\leq j}) = \tilde{\psi}_L^{\alpha_j}(F(\mathbf{x}_{\leq j})). \quad (\text{B.22})$$

This implies that the marginal probability satisfies $q(\mathbf{x}_{\leq j}) = q(F(\mathbf{x}_{\leq j}))$ after contracting over the index α_j , which then results in the correct symmetry on the conditional probabilities

$$q(x_j|\mathbf{x}_{<j}) = q(F(x_j)|F(\mathbf{x}_{<j})), \quad (\text{B.23})$$

as conditional probability is just the marginal probability normalized at site j . The phase, on the other hand,

$$\phi(\mathbf{x}) = \text{Arg} \sum_{\alpha} \prod_{i=1}^n \tilde{\psi}^{\alpha_{i-1}, \alpha_i}(x_i|\mathbf{x}_{<i}) = \text{Arg} \tilde{\psi}_L^{\alpha_n}(\mathbf{x}_{\leq n}), \quad (\text{B.24})$$

which satisfies the same function symmetry from Eq. B.22. \square

Corollary B.4.1 (\mathbb{Z}_2 Spin Flip Symmetry). *Autoregressive Neural TensorNet can realize \mathbb{Z}_2 spin flip symmetry such that the ANTN wavefunction is invariant under conjugation of the input.*

Proof. Spin flip symmetry exists for quantum chemistry systems that do not couple spin up and spin down electron, so that the wavefunction is invariant to inputs which spin up and down are flipped. (Barrett et al., 2022) has shown that autoregressive neural network can preserve \mathbb{Z}_2 spin flip symmetry as a function symmetry, which ANTN inherits. \square

Corollary B.4.2 (Discrete Abelian and Non-Abelian Symmetries). *Autoregressive Neural TensorNet can realize discrete Abelian and Non-Abelian symmetries.*

Proof. Gauge symmetry is a local symmetry such that the function is invariant under local transformation. (Luo et al., 2021b) has shown that autoregressive neural network can preserve discrete Abelian and non-Abelian symmetries as either the mask symmetry or the function symmetry, which ANTN inherits. \square

C Experimental Details and Reproducibility

We note that while the following details can be used to reproduce our results, addition adjustment may be possible to further improve our results.

Implementation. The transformer (Vaswani et al., 2017) used in this work is a decoder-only transformer implemented in (Luo et al., 2020), and the PixelCNN used is the gated PixelCNN (Van den Oord et al., 2016) implemented in (Chen et al., 2022) but without the channelwise mask. We will release the code following the publication of this work.

Hyperparameters. For the transformer in quantum state learning, we use 2 layers, 32 hidden dimensions and 16 attention heads, whereas for the PixelCNN in variational Monte Carlo, we use 7 layers with dilations 1, 2, 1, 4, 1, 2, and 1 for each layer, and 48 hidden dimensions.

Initialization. Throughout the experiment, we initialize the weight matrices of the last fully connected layer of the ARNN and ANTN to 0, and initialize the bias according to the following rule:

- The bias of ARNN is always randomly initialized.
- For the random Bell state learning, the bias of ANTN is randomly initialized
- For the rest of the experiment, the bias of ANTN is set to be 0.

The rest of the parameters of ARNN and ANTN are randomly initialized according to PyTorch (Paszke et al., 2019)’s default initialization scheme.

In addition, for the random Bell state learning experiment, we do not initialize the ANTN with MPS (and hence the random bias), whereas for the shallow random circuit learning experiment, we initialize the ANTN with an MPS that comes from explicit truncation of the full wavefunction, and for the variational Monte Carlo experiment, we initialize the ANTN with DMRG optimized MPS.

Optimization. Through the experiment, we use Adam optimizer with an initial learning rate of 0.01. For quantum state learning experiments, we train the ARNN and ANTN with full basis for 2000 iterations, where the learning rate is halved at iterations 600, 1200 and 1800. In case that the full basis cannot be computed in one pass due to GPU memory constraint, we divide the full basis into several batches and accumulates the gradient in each iteration. For variational Monte Carlo experiments, we train the ARNN and ANTN stochastically until the energy converges. During the training, we halve the learning rate at iterations 100, 500, 1000, 1800, 2500 and 4000. In each experiment, we choose the maximum batch size that can be fed into the GPU memory, while using accumulation steps to keep the effective batch size around 10000 throughout the training.

Transfer Learning. We in addition take advantage of transfer learning. For $J_2 = 0.2, 0.5$ and 0.8 , we begin from scratch with the 4×4 system. Then, an $N \times N$ system is initialized from an $(N - 2) \times (N - 2)$ system by keeping all but the weights in the last layer. Then, for other J_2 , the neural network is initialized from one of $J_2 = 0.2, 0.5$ and 0.8 that is closest to the current J_2 of the same system size by keeping all but the weights in the last layer. We find this allows the optimization to converge faster than always starting from scratch.

Computational Resources. The models are mainly trained using NVIDIA V100 GPUs with 32 GB memory and Intel Xeon Gold 6248 CPUs, with some models trained using NVIDIA A100 GPUs with 80 GB memory.

References

Barrett, T. D., Malyshev, A., and Lvovsky, A. Autoregressive neural-network wavefunctions for ab initio quantum chemistry. *Nature Machine Intelligence*, 4(4):351–358, 2022.

Capriotti, L., Fubini, A., Roscilde, T., and Tognetti, V. Ising transition in the two-dimensional quantum $j_1 - j_2$ heisenberg model. *Physical review letters*, 92(15):157202, 2004.

Carleo, G. and Troyer, M. Solving the quantum many-body problem with artificial neural networks. *Science*, 355(6325):602–606, 2017. doi: 10.1126/science.aag2302. URL <https://www.science.org/doi/10.1126/science.aag2302>.

Chen, Z., Luo, D., Hu, K., and Clark, B. K. Simulating 2+ 1d lattice quantum electrodynamics at finite density with neural flow wavefunctions. *arXiv preprint arXiv:2212.06835*, 2022.

Choo, K., Neupert, T., and Carleo, G. Two-dimensional frustrated $J_1 - J_2$ model studied with neural network quantum states. *Phys. Rev. B*, 100:125124, Sep 2019. doi: 10.1103/PhysRevB.100.125124. URL <https://link.aps.org/doi/10.1103/PhysRevB.100.125124>.

Deng, D.-L., Li, X., and Das Sarma, S. Quantum entanglement in neural network states. *Physical Review X*, 7(2), May 2017. ISSN 2160-3308. doi: 10.1103/physrevx.7.021021. URL <http://dx.doi.org/10.1103/PhysRevX.7.021021>.

Ferris, A. J. and Vidal, G. Perfect sampling with unitary tensor networks. *Phys. Rev. B*, 85:165146, Apr 2012. doi: 10.1103/PhysRevB.85.165146. URL <https://link.aps.org/doi/10.1103/PhysRevB.85.165146>.

Gao, X. and Duan, L.-M. Efficient representation of quantum many-body states with deep neural networks. *Nature Communications*, 8(1):662, Sep 2017. ISSN 2041-1723. doi: 10.1038/s41467-017-00705-2. URL <https://www.nature.com/articles/s41467-017-00705-2>.

Girvin, S. M. and Yang, K. *Modern condensed matter physics*. Cambridge University Press, 2019.

Greensmith, E., Bartlett, P. L., and Baxter, J. Variance reduction techniques for gradient estimates in reinforcement learning. *J. Mach. Learn. Res.*, 5:1471–1530, December 2004. ISSN 1532-4435.

Gutiérrez, I. L. and Mendl, C. B. Real time evolution with neural-network quantum states, 2020.

Hartmann, M. J. and Carleo, G. Neural-network approach to dissipative quantum many-body dynamics. *Phys. Rev. Lett.*, 122:250502, Jun 2019. doi: 10.1103/PhysRevLett.122.250502. URL <https://journals.aps.org/prl/abstract/10.1103/PhysRevLett.122.250502>.

Hermann, J., Schätzle, Z., and Noé, F. Deep neural network solution of the electronic schrödinger equation, 2019.

Hibat-Allah, M., Ganahl, M., Hayward, L. E., Melko, R. G., and Carrasquilla, J. Recurrent neural network wave functions. *Phys. Rev. Research*, 2:023358, Jun 2020. doi: 10.1103/PhysRevResearch.2.023358. URL <https://journals.aps.org/prresearch/abstract/10.1103/PhysRevResearch.2.023358>.

Huang, Y. and Moore, J. E. Neural network representation of tensor network and chiral states. *Phys. Rev. Lett.*, 127:170601, Oct 2021. doi: 10.1103/PhysRevLett.127.170601. URL <https://link.aps.org/doi/10.1103/PhysRevLett.127.170601>.

Lami, G., Carleo, G., and Collura, M. Matrix product states with backflow correlations. *Physical Review B*, 106(8), aug 2022. doi: 10.1103/physrevb.106.l081111. URL <https://doi.org/10.1103%2Fphysrevb.106.1081111>.

Lante, V. and Parola, A. The ising phase in the j1-j2 heisenberg model. *Physical Review*, 2006.

Levine, Y., Sharir, O., Cohen, N., and Shashua, A. Quantum entanglement in deep learning architectures. *Physical Review Letters*, 122(6), Feb 2019a. ISSN 1079-7114. doi: 10.1103/physrevlett.122.065301. URL <https://journals.aps.org/prl/abstract/10.1103/PhysRevLett.122.065301>.

Levine, Y., Sharir, O., Cohen, N., and Shashua, A. Quantum entanglement in deep learning architectures. *Physical review letters*, 122(6):065301, 2019b.

Lu, S., Gao, X., and Duan, L.-M. Efficient representation of topologically ordered states with restricted boltzmann machines. *Phys. Rev. B*, 99:155136, Apr 2019. doi: 10.1103/PhysRevB.99.155136. URL <https://journals.aps.org/prb/abstract/10.1103/PhysRevB.99.155136>.

Luo, D. and Clark, B. K. Backflow transformations via neural networks for quantum many-body wave functions. *Physical Review Letters*, 122(22), Jun 2019. ISSN 1079-7114. doi: 10.1103/physrevlett.122.226401. URL <https://journals.aps.org/prl/abstract/10.1103/PhysRevLett.122.226401>.

Luo, D., Chen, Z., Carrasquilla, J., and Clark, B. K. Autoregressive neural network for simulating open quantum systems via a probabilistic formulation, 2020.

Luo, D., Carleo, G., Clark, B. K., and Stokes, J. Gauge equivariant neural networks for quantum lattice gauge theories. *Physical review letters*, 127(27):276402, 2021a.

Luo, D., Chen, Z., Hu, K., Zhao, Z., Hur, V. M., and Clark, B. K. Gauge invariant autoregressive neural networks for quantum lattice models, 2021b. URL <https://arxiv.org/abs/2101.07243>.

Luo, D., Chen, Z., Carrasquilla, J., and Clark, B. K. Autoregressive neural network for simulating open quantum systems via a probabilistic formulation. *Phys. Rev. Lett.*, 128:090501, Feb 2022a. doi: 10.1103/PhysRevLett.128.090501. URL <https://link.aps.org/doi/10.1103/PhysRevLett.128.090501>.

Luo, D., Yuan, S., Stokes, J., and Clark, B. K. Gauge equivariant neural networks for 2+ 1d u (1) gauge theory simulations in hamiltonian formulation. *arXiv preprint arXiv:2211.03198*, 2022b.

Marshall, W. Antiferromagnetism. *Proceedings of the Royal Society of London. Series A, Mathematical and Physical Sciences*, 232(1188):48–68, 1955. ISSN 00804630. URL <http://www.jstor.org/stable/99682>.

Nagy, A. and Savona, V. Variational quantum monte carlo method with a neural-network ansatz for open quantum systems. *Phys. Rev. Lett.*, 122:250501, Jun 2019. doi: 10.1103/PhysRevLett.122.250501. URL <https://journals.aps.org/prl/abstract/10.1103/PhysRevLett.122.250501>.

Nomura, Y. and Imada, M. Dirac-type nodal spin liquid revealed by refined quantum many-body solver using neural-network wave function, correlation ratio, and level spectroscopy. *Physical Review X*, 11(3), aug 2021. doi: 10.1103/physrevx.11.031034. URL <https://doi.org/10.1103%2Fphysrevx.11.031034>.

Oseledets, I. V. Tensor-train decomposition. *SIAM Journal on Scientific Computing*, 33(5):2295–2317, 2011. doi: 10.1137/090752286. URL <https://doi.org/10.1137/090752286>.

Paszke, A., Gross, S., Massa, F., Lerer, A., Bradbury, J., Chanan, G., Killeen, T., Lin, Z., Gimelshein, N., Antiga, L., et al. Pytorch: An imperative style, high-performance deep learning library. In *Advances in neural information processing systems*, pp. 8026–8037, 2019.

Pfau, D., Spencer, J. S., Matthews, A. G. D. G., and Foulkes, W. M. C. Ab initio solution of the many-electron schrödinger equation with deep neural networks. *Phys. Rev. Research*, 2:033429, Sep 2020. doi: 10.1103/PhysRevResearch.2.033429. URL <https://journals.aps.org/prresearch/abstract/10.1103/PhysRevResearch.2.033429>.

Preskill, J. Quantum computing 40 years later. *arXiv preprint arXiv:2106.10522*, 2021.

Schmitt, M. and Heyl, M. Quantum many-body dynamics in two dimensions with artificial neural networks. *Physical Review Letters*, 125(10), Sep 2020. ISSN 1079-7114. doi: 10.1103/physrevlett.125.100503. URL <https://journals.aps.org/prl/abstract/10.1103/PhysRevLett.125.100503>.

Sharir, O., Levine, Y., Wies, N., Carleo, G., and Shashua, A. Deep autoregressive models for the efficient variational simulation of many-body quantum systems. *Physical Review Letters*, 124(2), jan 2020. doi: 10.1103/physrevlett.124.020503. URL <https://doi.org/10.1103%2Fphysrevlett.124.020503>.

Sharir, O., Shashua, A., and Carleo, G. Neural tensor contractions and the expressive power of deep neural quantum states, 2021.

Van den Oord, A., Kalchbrenner, N., Espeholt, L., Vinyals, O., Graves, A., et al. Conditional image generation with pixelcnn decoders. *Advances in neural information processing systems*, 29, 2016.

Vaswani, A., Shazeer, N., Parmar, N., Uszkoreit, J., Jones, L., Gomez, A. N., Kaiser, Ł., and Polosukhin, I. Attention is all you need. *Advances in neural information processing systems*, 30: 5998–6008, 2017.

Verstraete, F. and Cirac, J. I. Renormalization algorithms for quantum-many body systems in two and higher dimensions, 2004. URL <https://arxiv.org/abs/cond-mat/0407066>.

Vicentini, F., Biella, A., Regnault, N., and Ciuti, C. Variational neural-network ansatz for steady states in open quantum systems. *Physical Review Letters*, 122(25), Jun 2019. ISSN 1079-7114. doi: 10.1103/physrevlett.122.250503. URL <https://journals.aps.org/prl/abstract/10.1103/PhysRevLett.122.250503>.

Vicentini, F., Hofmann, D., Szabó, A., Wu, D., Roth, C., Giuliani, C., Pescia, G., Nys, J., Vargas-Calderón, V., Astrakhantsev, N., and Carleo, G. NetKet 3: Machine learning toolbox for many-body quantum systems. *SciPost Physics Codebases*, aug 2022. doi: 10.21468/scipostphyscodeb.7. URL <https://doi.org/10.21468/scipostphyscodeb.7>.

Vidal, G. Efficient classical simulation of slightly entangled quantum computations. *Physical Review Letters*, 91(14), oct 2003. doi: 10.1103/physrevlett.91.147902. URL <https://doi.org/10.1103/physrevlett.91.147902>.

Vidal, G. Efficient simulation of one-dimensional quantum many-body systems. *Physical Review Letters*, 93(4), jul 2004. doi: 10.1103/physrevlett.93.040502. URL <https://doi.org/10.1103/physrevlett.93.040502>.

Vidal, G. Entanglement renormalization. *Phys. Rev. Lett.*, 99:220405, Nov 2007. doi: 10.1103/PhysRevLett.99.220405. URL <https://link.aps.org/doi/10.1103/PhysRevLett.99.220405>.

Vieijra, T., Casert, C., Nys, J., De Neve, W., Haegeman, J., Ryckebusch, J., and Verstraete, F. Restricted boltzmann machines for quantum states with non-abelian or anyonic symmetries. *Physical Review Letters*, 124(9), Mar 2020. ISSN 1079-7114. doi: 10.1103/physrevlett.124.097201. URL <https://journals.aps.org/prl/abstract/10.1103/PhysRevLett.124.097201>.

Westerhout, T., Astrakhantsev, N., Tikhonov, K. S., Katsnelson, M. I., and Bagrov, A. A. Generalization properties of neural network approximations to frustrated magnet ground states. *Nature Communications*, 11(1):1593, Mar 2020. ISSN 2041-1723. doi: 10.1038/s41467-020-15402-w. URL <https://doi.org/10.1038/s41467-020-15402-w>.

White, S. R. Density matrix formulation for quantum renormalization groups. *Physical review letters*, 69(19):2863, 1992.

Wu, D., Rossi, R., Vicentini, F., and Carleo, G. From tensor network quantum states to tensorial recurrent neural networks. *arXiv preprint arXiv:2206.12363*, 2022.

Yoshioka, N. and Hamazaki, R. Constructing neural stationary states for open quantum many-body systems. *Phys. Rev. B*, 99:214306, Jun 2019. doi: 10.1103/PhysRevB.99.214306. URL <https://journals.aps.org/prb/abstract/10.1103/PhysRevB.99.214306>.